




Article

Synthesis and Characterization of Novel Copper(II)-Sunitinib Complex: Molecular Docking, DFT Studies, Hirshfeld Analysis and Cytotoxicity Studies

Facundo Tarasi ¹, Priscila Ailín Lanza ², Valeria Ferretti ³, Gustavo Alberto Echeverría ⁴ , Oscar Enrique Piro ⁴, Maximiliano Cacicedo ⁵ , Stephan Gehring ⁵, Ignacio Esteban León ^{3,6,*} and María Soledad Islas ^{1,*} 

¹ Departamento de Química y Bioquímica, Facultad de Ciencias Exactas y Naturales, Universidad Nacional de Mar del Plata, Mar del Plata 7600, Argentina; ftarasi@mdp.edu.ar

² QUIAMM (Grupo de Investigación en Química Analítica y Modelado Molecular), Vinculado a INBIOTEC-CONICET (Instituto de Investigaciones en Biodiversidad y Biotecnología), Departamento de Química y Bioquímica, Facultad de Ciencias Exactas y Naturales, Universidad Nacional de Mar del Plata, Mar del Plata 7600, Argentina; planza@mdp.edu.ar

³ CEQUINOR (UNLP, CCT-CONICET La Plata, Asociado a CIC), Departamento de Química, Facultad de Ciencias Exactas, Universidad Nacional de La Plata. Blvd. 120 N° 1465, La Plata 1900, Argentina; vferretti@med.unlp.edu.ar

⁴ Departamento de Física, Facultad de Ciencias Exactas, Universidad Nacional de La Plata e IFLP (CONICET, CCT-La Plata), C.C. 67, La Plata 1900, Argentina; gualech@gmail.com (G.A.E.); piro@fisica.unlp.edu.ar (O.E.P.)

⁵ Laboratory of Pediatric Immunology and Infectious Diseases, Children's Hospital, University Medical Center, Johannes Gutenberg Mainz University, 55131 Mainz, Germany; mcacicedo@uni-mainz.de (M.C.); Stephan.Gehring@uni-mainz.de (S.G.)

⁶ Cátedra de Fisiopatología, Departamento de Ciencias Biológicas, Facultad de Ciencias Exactas, Universidad Nacional de La Plata. 47 y 115, La Plata 1900, Argentina

* Correspondence: ileon@biol.unlp.edu.ar (I.E.L.); msislas@mdp.edu.ar (M.S.I.)



Citation: Tarasi, F.; Lanza, P.A.; Ferretti, V.; Echeverría, G.A.; Piro, O.E.; Cacicedo, M.; Gehring, S.; León, I.E.; Islas, M.S. Synthesis and Characterization of Novel Copper(II)-Sunitinib Complex: Molecular Docking, DFT Studies, Hirshfeld Analysis and Cytotoxicity Studies. *Inorganics* **2022**, *10*, 3. <https://doi.org/10.3390/inorganics10010003>

Academic Editor: Isabel Correia

Received: 29 November 2021

Accepted: 20 December 2021

Published: 22 December 2021

Publisher's Note: MDPI stays neutral with regard to jurisdictional claims in published maps and institutional affiliations.



Copyright: © 2021 by the authors. Licensee MDPI, Basel, Switzerland. This article is an open access article distributed under the terms and conditions of the Creative Commons Attribution (CC BY) license (<https://creativecommons.org/licenses/by/4.0/>).

Abstract: The main goal of this work was to report the synthesis, characterization, and cytotoxicity study of a novel copper(II)-sunitinib complex, CuSun. It has been synthesized and characterized in solid state and in solution by different methods (such as DFT, FTIR, Raman, UV-vis, EPR, NMR, etc.). The solid-state molecular structure of trichlorosunitinibcopper(II), where sunitinib: *N*-[2-(diethylamino)ethyl]-5-[(*Z*)-(5-fluoro-2-oxo-1H-indol-3-ylidene)methyl]-2,4-dimethyl-1H-pyrrole-3-carboxamide, for short Cu(Sun)Cl₃, was determined by X-ray diffraction. It crystallizes in the triclinic space group P-1 with *a* = 7.9061(5) Å, *b* = 12.412(1) Å, *c* = 13.7005(8) Å, α = 105.021(6)°, β = 106.744(5)°, γ = 91.749(5)°, and *Z* = 2 molecules per unit cell. Also, we have found π - π interactions and classic and non-classic H-bonds in the crystal structure by using Hirshfeld surface analysis. In the speciation studies, the complex has dissociated in protonated sunitinib and chlorocomplex of copper(II), according to ¹HNMR, EPR, UV-vis and conductimetric analysis. Molecular docking of the complex in both, ATP binding site and allosteric site of VEGFR2 have shown no improvement in comparison to the free ligand. Besides, cytotoxicity assay on HepG2 cell line shows similar activity for complex and ligand in the range between 1–25 μ M supporting the data obtained from studies in solution.

Keywords: sunitinib; copper; coordination complexes; docking; VEGFR2

1. Introduction

Cancer is one of the principal motives of death worldwide [1]. Several tyrosine kinase receptors have been shown to play key roles in tumor growth and angiogenesis [2]. The most important are platelet-derived growth factor receptors (PDGFRs, which include PDGFR α and PDGFR β), fibroblast growth factor receptors, and vascular endothelial growth factor receptors (VEGFRs which include VEGFR1 and VEGFR2). Therefore, many strategies to inhibit the cell signaling action of VEGF are explored using antibodies [3–5] or VEGFR

antagonists [6–8]. In this sense, Sunitinib (sunitinib malate; SU11248; SUTENT™; Pfizer Inc, New York, NY, USA) is a novel oral multitargeted tyrosine kinase inhibitor with antitumor and antiangiogenic activities that it has been identified as a potent inhibitor of VEGFR1, VEGFR2, PDGFR α , and PDGFR β [9,10]. Many scientific reports [11,12] supported the idea that VEGF is the key mediator of angiogenesis in cancer, in which it is up-regulated by oncogene expression, hypoxia and several growth factors. The generation and regulation of VEGF and other growth factors by the tumor results in the ‘angiogenic switch’, where new vasculature is formed in and around the tumor, allowing it to grow exponentially. Particularly, VEGFR2 is one of most active VEGF receptors that promote tumorigenesis and metastasis in gastric, lung, breast and liver cancers [13,14].

Sunitinib (Sun, Figure 1) is a yellow non-hygroscopic powder which low pH-dependent solubility in aqueous media, it is achiral and exhibits polymorphism [15]. It was formally approved by the US Food and Drug Administration (FDA) for the indications of treating renal cell carcinoma (RCC) and imatinib-resistant gastrointestinal stromal tumor (GIST). Currently, this compound exhibited anticancer activity on in vitro and in vivo models of thyroid [16], liver and breast [17–19] and it shows to be efficacious as single agent in the treatment of a broad range of solid tumors such as RCC, GIST and pancreatic neuroendocrine tumors (pNET) [20–22].

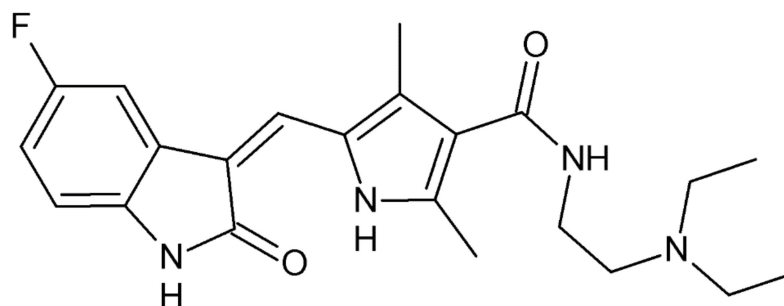


Figure 1. Structure of Sunitinib (Sun). IUPAC name: *N*-[2-(diethylamino)ethyl]-5-[(*Z*)-(5-fluoro-1,2-dihydro-2-oxo-3H-indol-3-ylidene)methyl]-2,4-dimethyl-1H-pyrrole-3-carboxamide.

Metallodrugs are a family of antineoplastic agents largely used in the treatment of several types of cancers like lung, prostate, liver, among others [23]. Platinum compounds (cisplatin, carboplatin and oxaliplatin) are the most successful compounds derived from metals use in clinic in the treatment of many tumors [24]. However, chemoresistance to platinum is one of the most relevant clinical problems in the treatment [25] and has led to many scientists focusing efforts on the development of novel non-platinum-based compounds [26].

In this sense, copper compounds show promising anticancer effects on different solid tumors [27–31]. Moreover, the anti-angiogenic and anti-metastatic properties of mono-nuclear copper (II) complexes have been reported [32–34].

As part of our project, we have synthesized Cu(II) coordination complex with sunitinib (CuSun). An extensive experimental and theoretical characterization of the compound was done. The solid-state molecular structure has been determined by single crystal X-ray diffraction methods. Bands observed in Fourier Transform Infrared (FTIR), Raman and electronic absorption spectra were assigned with the aid of the results from computational methods based on the Density Functional Theory (DFT). Docking studies were performed with the goal of elucidating the interaction between CuSun and VEGFR2. Finally, we have investigated the effects of Sun, CuSun and copper cation on HepG2 hepatocarcinoma cell line.

2. Results and Discussion

2.1. Synthesis and Characterization

Synthesis of complex CuSun: $[\text{CuCl}_3(\text{HSun})]$ or $\text{CuCl}_3\text{C}_{22}\text{H}_{28}\text{FN}_4\text{O}_2$ (Mw: 569.4 g/mol) was obtained from Sun (0.25 mmol in 40 mL of acetone) that was dissolved under continuous stirring by heating the solution in a water bath at 50 °C. Then, a solution of $\text{CuCl}_2 \cdot 2\text{H}_2\text{O}$ (1.25 mmol in 10 mL of acetone) was added to the previous yellow solution. The brownish solution obtained was slowly evaporated at room temperature, and purple-brownish crystals suitable for X-ray studies were obtained in the mother liquor after a day (yield 57%). UV-visible spectrum (in dimethyl sulfoxide, DMSO): 270 nm ($\epsilon = 2.2 \times 10^4 \text{ M}^{-1} \text{ cm}^{-1}$), 478 nm ($\epsilon = 6.0 \times 10^4 \text{ M}^{-1} \text{ cm}^{-1}$), 920 nm ($\epsilon = 94 \text{ M}^{-1} \text{ cm}^{-1}$). Diffuse reflectance spectrum: CuSun, single crystal, 492 nm and 818 nm (Figure S1). $^1\text{HNMR}$ (DMSO- d_6): 13.74 (s, 1H), 10.92 (s, 1H), 9.84 (br, 1H), 7.79 (m, 1H), 7.76–7.79 (d, 1H), 7.73 (s, 1H), 6.91–6.97 (m, 1H), 6.84–6.87 (m, 1H), 3.52–3.60 (m, 2H), 3.20–3.24 (m, 6H), 2.48 (s, 3H), 2.46 (s, 3H), 1.23–1.27 (t, 6H) (Figure S2).

The complex, CuSun, is slightly soluble in water, ethanol, acetonitrile, and chloroform, but soluble in DMSO. In this last solvent, it dissociates in different ionic species. The average molar conductivity (Λ_M) measured was $53.7 \Omega^{-1} \text{ cm}^2 \text{ mol}^{-1}$ (concentrations in the range 1.3 to 4.3 mmol L^{-1}). If we suppose complete dissociation, this value is in agreement with 1:1 electrolyte in DMSO [35]. Besides, by UV-vis spectroscopy, we have observed the same maximum at 920 nm in DMSO for both, $\text{CuCl}_2 \cdot 2\text{H}_2\text{O}$ and CuSun. Herein, we propose that these spectra are in agreement with the formation of the complex $[\text{CuCl}_3(\text{DMSO})]^-$ [36]. No changes in the complex spectrum have been observed in 60 min (data not shown). $^1\text{HNMR}$ in (DMSO- d_6) have shown almost the same pattern for both sunitinib (Figure S3) and CuSun (Figure S2). The main difference is in a broad singlet observed at 9.84 ppm for the complex, that corresponds to a proton bonded to the amine group (Figure S2). The spectrum of CuSun was similar to that reported for sunitinib malate [37,38], since in these cases Sun is found as HSun^+ . Lastly, we have measured the EPR spectra of a solution of CuSun and $\text{CuCl}_2 \cdot 2\text{H}_2\text{O}$ in DMSO at room temperature and we have found similar spectra in both cases (Figure S4). Taking these results into account, we propose that CuSun complex, once dissolved in DMSO, dissociates mainly in $[\text{CuCl}_3(\text{DMSO})]^-$ (further dissociation are possible according to [36]) and HSun^+ .

2.2. Crystal Structure

An Oak Ridge Thermal Ellipsoid Plot (ORTEP) [39] draw of the complex is shown in Figure 2, with the crystal data and structure refinement results in Table 1 and bond distances and angles around copper(II) in Table 2. Copper ion is in a distorted tetrahedral environment, CuOCl_3 , coordinated by a sunitinib molecule acting as a monodentate ligand through its oxindole carbonyl group [$d(\text{Cu}-\text{O}) = 2.082(2) \text{ \AA}$] and by three chlorine ions [$\text{Cu}-\text{Cl}$ bond distances from 2.179(1) to 2.231(1) \AA]. The sunitinib ligand is positively charged through protonation at the amine N-atom.

Because extended π -bond delocalization, the [(Z)-(5-fluoro-2-oxo-1H-indol-3-ylidene)methyl]-2,4-dimethyl-1H-pyrrole fragment is nearly planar (rms deviation of non-H atoms from the best least-squares plane equal to 0.0274 \AA). Planarity is also favored by an intra-ligand H-bond linking the pyrrole $>\text{N}-\text{H}$ and oxindole $>\text{C}=\text{O}$ groups [$d(\text{N} \cdots \text{O}) = 2.728(3) \text{ \AA}$, $d(\text{H} \cdots \text{O}) = 1.95(2) \text{ \AA}$ and $\angle(\text{N}-\text{H} \cdots \text{O}) = 151(3)^\circ$]. The metal lay close onto this plane (at 0.4717 \AA). The molecule is further stabilized by another intra-ligand H-bond, now involving as donor the amine NH^+ group and as acceptor the amide $>\text{C}=\text{O}$ carbonyl group [$d(\text{N} \cdots \text{O}) = 2.666(4) \text{ \AA}$, $d(\text{H} \cdots \text{O}) = 1.87(2) \text{ \AA}$ and $\angle(\text{N}-\text{H} \cdots \text{O}) = 157(3)^\circ$] and also by an intra-complex H-bond involving the NH group of the 5-fluoro oxindole fragment and a chlorine ion [$d(\text{N} \cdots \text{Cl}) = 3.240(3) \text{ \AA}$, $d(\text{H} \cdots \text{Cl}) = 2.59(4) \text{ \AA}$ and $\angle(\text{N}-\text{H} \cdots \text{Cl}) = 142(3)^\circ$]. Additional details of the H-bonding structure in the crystal are given in the Supplementary Table S1.

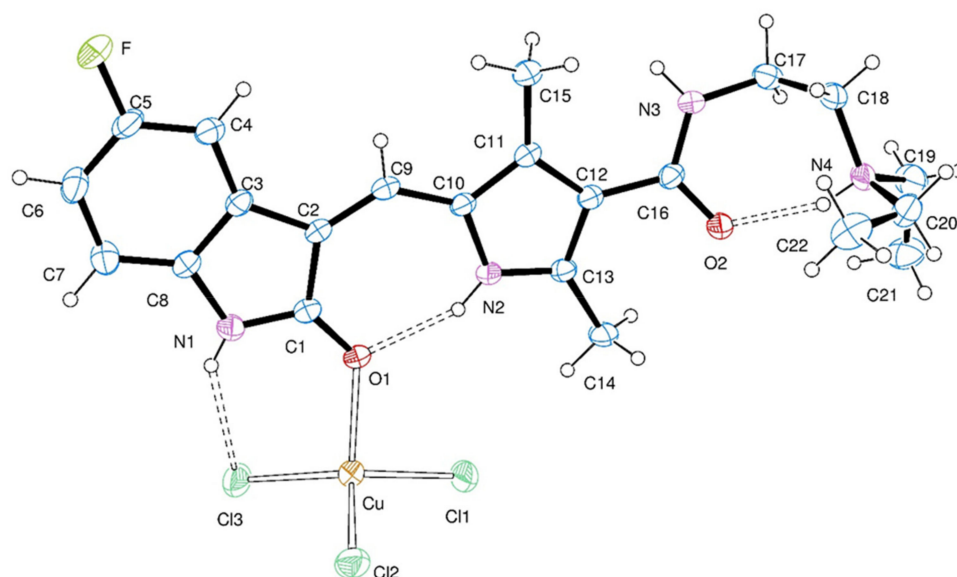


Figure 2. View of trichlorosunitinibcopper(II) (CuSun) molecule, showing the labeling of the non-H atoms and their displacement ellipsoids at the 30% probability level. Copper-ligand bonds are indicated by open lines and intra-molecular H-bonds by dashed lines.

Table 1. Crystal data and structure refinement results for trichlorosunitinibcopper(II) (CuSun).

Empirical formula	C ₂₂ H ₂₈ Cl ₃ Cu F N ₄ O ₂	
Formula weight	569.37	
Temperature	293(2) K	
Wavelength	0.71073 Å	
Crystal system	Triclinic	
Space group	P-1	
Unit cell dimensions	a = 7.9061(5) Å b = 12.412(1) Å c = 13.7005(8) Å	α = 105.021(6)° β = 106.744(5)° γ = 91.749(5)°
Volume	1235.4(2) Å ³	
Z, density (calculated)	2, 1.531 Mg/m ³	
Absorption coefficient	1.243 mm ⁻¹	
F(000)	586	
Crystal size	0.405 × 0.163 × 0.059 mm ³	
θ-range for data collection	3.208 to 29.153°	
Index ranges	−10 ≤ h ≤ 10, −16 ≤ k ≤ 16, −18 ≤ l ≤ 15	
Reflections collected	9998	
Independent reflections	5335 [R(int) = 0.0310]	
Observed reflections [I > 2σ(I)]	3879	
Completeness to θ = 25.242°	99.8%	
Refinement method	Full-matrix least-squares on F ²	
Data/restraints/parameters	5335/3/366	
Goodness-of-fit on F2	1.031	
Final R indices ^a [I > 2σ(I)]	R1 = 0.0474, wR2 = 0.1112	
R indices (all data)	R1 = 0.0726, wR2 = 0.1275	
Largest diff. peak and hole	0.458 and −0.404 e.Å ⁻³	

^a $R_1 = \sum ||F_o| - |F_c|| / \sum |F_o|$, $wR_2 = [\sum w(|F_o|^2 - |F_c|^2)^2 / \sum w(|F_o|^2)^2]^{1/2}$.

Table 2. Bond lengths [Å] and angles [°] around copper in for trichlorosunitinibcopper(II) (CuSun).

Bond Lengths [Å]		Angles [°]	
O(1)-Cu	2.082(2)	O(1)-Cu-Cl(1)	93.48(7)
Cu-Cl(1)	2.179(1)	O(1)-Cu-Cl(2)	121.29(8)
Cu-Cl(2)	2.193(1)	Cl(1)-Cu-Cl(2)	104.24(4)
Cu-Cl(3)	2.231(1)	O(1)-Cu-Cl(3)	100.23(7)
		Cl(1)-Cu-Cl(3)	133.95(5)
		Cl(2)-Cu-Cl(3)	105.39(5)

2.3. Hirshfeld Surface

Hirshfeld surface analysis can be a valuable tool in the study of intermolecular interactions in a crystalline solid [40]. With the aim of identifying the intermolecular contacts present in the solid phase structure of the CuSun complex, we have mapped the d_{norm} function on the Hirshfeld surface (Figure 3a,b). Blue regions correspond to distances greater than the sum of the van der Waals radii for the corresponding atoms, while the red ones show smaller distances. Eight red dots can be seen on the surface, four of them are considerably larger and more intense than the others.

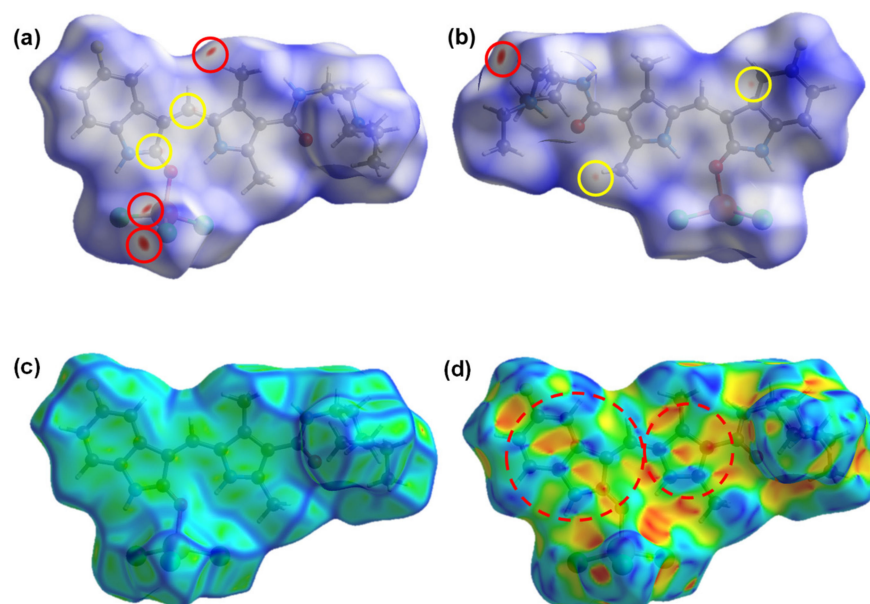


Figure 3. Front (a) and back (b) view of the Hirshfeld surface of the CuSun complex mapped with the d_{norm} function, from -0.10 to 1.68 (the red and yellow circles enclose regions with intermolecular contacts) and Hirshfeld surface of the CuSun complex mapped with (c) curvedness (values from -4.0 to 0.4), and (d) shape index (values from -1.0 to 1.0 , the circles show regions indicative of π -stacking interactions).

The most intense dots (in red circles in Figure 3a,b) are due to close contacts of the C-H/Cl type. These contacts seem to suggest the existence of non-classical hydrogen bonds of the C-H \cdots Cl type that would stabilize the crystal packing. On the other hand, the remaining dots (in yellow circles, Figure 3a,b), are smaller, less intense, and in different regions of the aromatic system of the sunitinib molecule. They represent the contacts of C/C type.

In addition, the Hirshfeld surface mapped with the curvature function (Figure 3c) has shown green patches, corresponding to relatively flat regions, separated by dark blue edges, corresponding to positive curvatures. The presence of these flat regions allows us to suggest the existence of π -stacking interactions between the conjugated π systems of different molecules. This can be corroborated by analyzing the shape index (Figure 3d), which is indicative of the local topology of the surface: red regions are cavities, while the

blue ones represent bumps. This function is commonly used to identify π - π interactions in aromatic systems, since they appear as areas of the surface with clusters of small, approximately triangular, red and blue regions, which correspond to the embedding of the molecules.

Fingerprint plots for the CuSun complex (Figure S5) show that the greatest contribution to the Hirshfeld surface area arises from intramolecular contacts of the H/H type (38.6%), a fairly common feature in compounds where H is the most abundant atom type [41]. However, the second prominent contact is H/Cl, with almost 30%. This has reinforced the hypothesis that non-classical C-H \cdots Cl hydrogen bonds may have a role in the stabilization of the structure of the complex in solid phase. In addition, a non-negligible number of H/F type contacts is observed. Both the C/C and C/N contacts are in the same region of the fingerprint plot, with (d_i , d_e) \sim 1.8–2.0 Å. This is a typical range of interplanar spacing for aromatic hydrocarbons associated with the presence of π -stacking interactions in their crystal structure [40]. The contacts mentioned above, represent 92.8% of the total; 7.2% are contacts between the remaining elements. Individually, they represented less than 5% of the total.

Herein, it is proposed that the existence of the π -stacking interactions and non-classic H bonds have an important contribution in the stability of the solid crystalline structure. On the contrary, the lack of this interactions in solution could be one of the reasons of the instability and further dissociation as described in Section 2.1.

2.4. Vibrational Spectroscopy

FTIR (Figure S6) and Raman (Figure S7) spectra were measured for CuSun and were compared with FTIR of sunitinib (the Raman spectrum of this ligand have exhibited fluorescence in our conditions and no bands were observed). In addition, vibrational frequencies calculated from the optimized geometries, and multiplied by a scaling factor of 0.9530 as suggested in the literature for the level of theory used [42], are shown for sunitinib and CuSun complex in Table 3. The assignments for the ligand are in agreement with literature [43].

The absorption in the range 4000–2000 cm^{-1} corresponds to the stretching vibrations of the N-H and C-H bonds. In particular, the broad band with maxima in 3422, 3284 cm^{-1} and a shoulder in 3178 cm^{-1} observed in the experimental FTIR spectrum of Sun has been assigned to NH stretching of the different groups in the molecule. A broad band between 3600–2500 cm^{-1} was observed in CuSun, similar to the band reported in sunitinib malate [44], where Sun is also protonated (as HSun⁺). There is only one intense band observed in 2790 cm^{-1} assigned to NH protonated, and discrete bands for the remain NH stretching (3445 (oxindole), 3436 (pyrrole) and 3387 cm^{-1} (amide)). Also, in CuSun, calculated CH stretching frequencies were between 3076–3060 cm^{-1} for C(sp²)-H and 3030–2908 cm^{-1} for C(sp³)-H.

Then, in the region from 1700 to 1500 cm^{-1} , several changes have been observed, mainly due to C=O, C=N and C=C stretching modes. For sunitinib, the carbonyl stretching mode of oxindole and amide groups were found in the same region, at 1677 cm^{-1} . This is between the two bands calculated, 1685 cm^{-1} for oxindole (coupled to other vibrational modes) and 1656 cm^{-1} for amide group. In the complex, the polarization produced in C=O bond due to the intramolecular hydrogen bonding (in amide moiety) or coordination to the metal center (in oxindole moiety) leads to an elongation of the C=O bond, and therefore, a shifting in the stretching modes to lower frequencies (Figure S6). In CuSun, the carbonyl stretching modes were found at 1645 cm^{-1} (oxindole) and 1615 cm^{-1} (amide) with strong intensity in FTIR (1649 and 1615 cm^{-1} in Raman, with a lower intensity, as expected). In this case, the calculated frequencies were 1668 cm^{-1} (also coupled to other vibrational modes) and 1596 cm^{-1} . On the other hand, C=N and C=C stretching modes have shown several shifts but, since both molecules (sunitinib and CuSun) present extended π -conjugated systems, many bands are assigned to combined vibrational modes. Tentative assignments in this region are shown also in Table 3, in agreement with calculated frequencies.

Table 3. Comparison of the main changes observed in the experimental and calculated vibrational frequencies, assignments and FTIR and Raman intensities for sunitinib (Sun) and its copper(II) complex (CuSun). Wavenumbers are in cm^{-1} and the experimental intensities are relative.

Tentative Assignations	Sun/ cm^{-1}		CuSun/ cm^{-1}		
	FTIR	Calculated	FTIR	Raman	Calculated
$\nu(\text{N-H})_a$	3455 (w),	3516 (w)	3422 (br,s)	-	3387 (w)
$\nu(\text{N-H})_o$	3300 (m),	3506 (w)	3284 (br,s)	-	3445 (m)
$\nu(\text{N-H})_p$	3228 (m)	3160 (m)	3178 (sh,m)	-	3436 (w)
$\nu(\text{N-H})_k$	-	-	3600–2500 * (m, vb)	-	2790 (s)
$\nu(\text{C-H})_{o,en,p}$	3138–3078 (w)	3076–3030 (w)	3048 * (w)	-	3076–3060 (w)
$\nu(\text{C-H})_{e,m}$	2969–2814 (m)	3004–2787 (m)	2983–2853 * (m)	-	3030–2908 (m)
$\nu(\text{C=O})_o + \nu(\text{C=C})_{en} + \delta(\text{CNH})_o$	1677 (s)	1685 (s)	1645 (s)	1649 (w)	1668 (s)
$\nu(\text{C=O})_a$		1656 (s)	1615 (s)	1615 (w)	1596 (s)
$\nu(\text{C=C})_{o,en} + \delta(\text{CNH})_{a,p} + \nu(\text{CN})_{o,p}$	1589 (s), 1543 (s), 1480 (m)	1570 (s), 1541 (m), 1504 (m)	1564 (s), 1536 (s), 1513 (m)	1553 (s), 1530 (m), 1512 (sh)	1577 (s), 1552 (m), 1506 (m)
$\delta(\text{CCH})_o + \delta(\text{CCC})_{o,p}$	1445 (m)	1462 (m)	1478 (m)	1481 (w), 1460 (w)	1463 (m)
$\delta(\text{HCH})_{e,m}$	1385 (w)	1409 (w)	1427 (m)	1428 (m)	1408 (w)
$\nu(\text{CN})_o + \delta(\text{HCC})_{en}$	1330 (s)	1304 (m)	1319 (s)	1300 (s)	1315 (m)
$t(\text{HCCH})_o + \omega(\text{CH}_2)_e$	1295 (m)	1276 (s)	1261 (w)	1250 (m)	1260 (w)
$\nu(\text{CN})_o + \delta(\text{HCC})_o$	1190 (m)	1160 (m)	1193 (m)	1190 (m)	1169 (w)
$\nu(\text{Cu-Cl})$	-	-	-	226 (m)	338 (w)–251 (w)

Subindex, a: amide; o: oxindole; p: pyrrole; k: amine group; en: methylene bridge; e: ethyl group; m: methyl group. Vibrational modes, ν : stretching; δ : bending in-plane; ω : wagging; t: twisting. Intensity, s: strong; m: medium; w: weak; br: broad; vb: very broad; sh: shoulder. * No clear assignation could be done because of the width.

Lastly, in the region below 1500 cm^{-1} , there were only slight changes between ligand and complex in the FTIR. Related to Cu-ligand stretching modes, we have observed some bands in Raman spectrum below 400 cm^{-1} (Figure S7). We have assigned the band in 226 cm^{-1} to Cu-Cl stretching, while no Cu-O stretching was observed. Since there are three different Cu-Cl bonds, with different lengths, the calculated values were between 338 y 251 cm^{-1} , while Cu-O was expected at 157 cm^{-1} .

2.5. Molecular Docking with VEGFR2

In order to assess the effects of sunitinib complexation on the activity of this compound on tyrosine kinase receptors, we have performed molecular docking simulations by selecting VEGFR2 as a significant physiological target.

In addition to CuSun, sunitinib in its free form was docked to the VEGFR2, for the purpose of estimating its binding energy. Due to the fact that this molecule has an amino group with a $\text{pKa} \sim 10$ [45], the main form present under physiological conditions should be the HSun^+ cation. Nevertheless, and for the sake of completeness, we have carried out the docking methodology using the protonated form (HSun^+), as well as, the basic one (Sun). Figure 4a,b show the lowest energy conformations found for HSun^+ and CuSun with VEGFR2, respectively. The results for the three ligands, Sun, HSun^+ , and CuSun, are shown in Table 4.

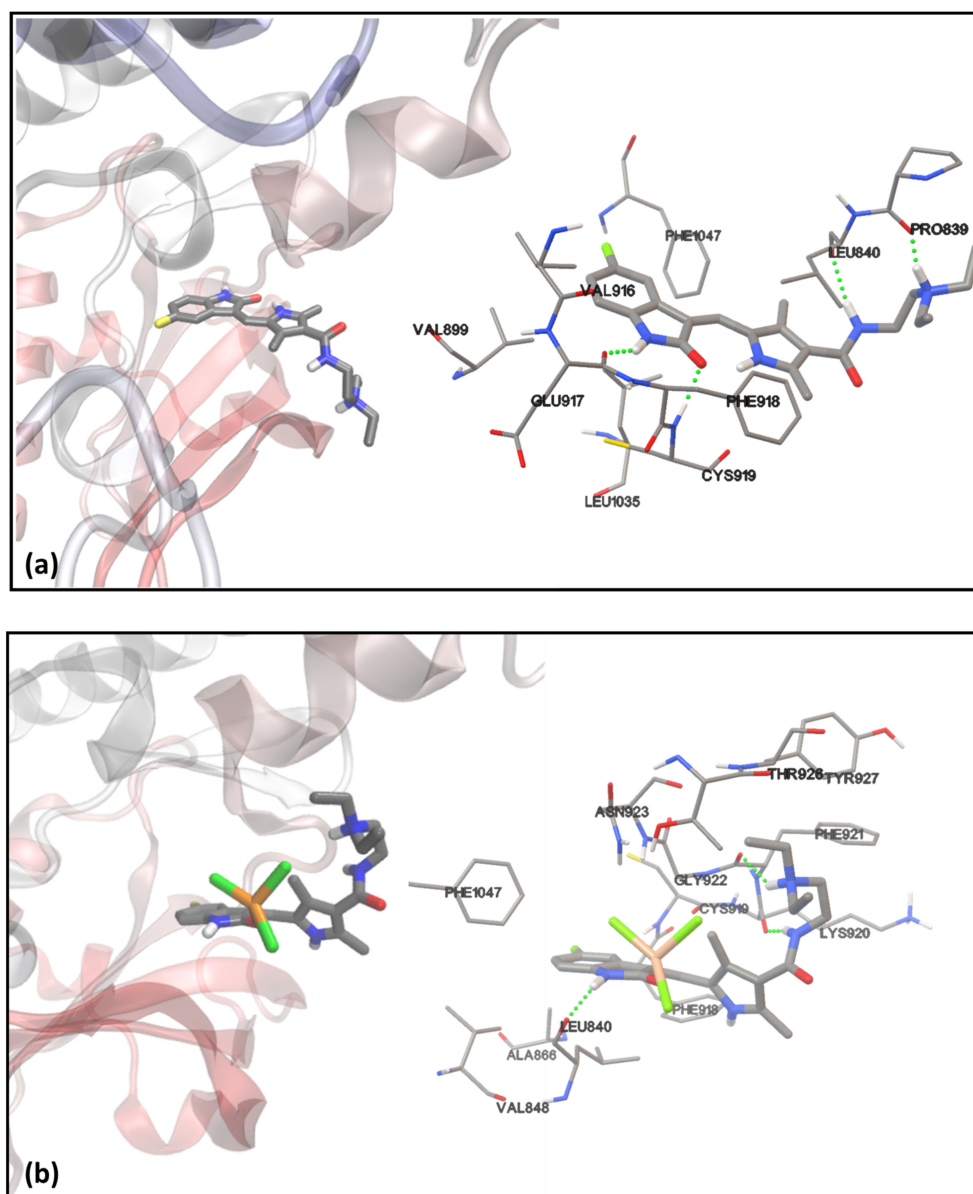


Figure 4. Left: Most favorable binding mode in the ATP binding pocket of the tyrosine kinase domain of VEGFR2 for (a) HSun⁺ and (b) CuSun. Right: Residues that interact with the ligand, through close contacts or through hydrogen bonds (shown as green dots) for (a) HSun⁺ and (b) CuSun.

Table 4. Binding energies (kcal mol^{−1}) and inhibition constants (K_i, μM) for the lowest energy conformations obtained by molecular docking, with VEGFR2 as rigid receptor and Sun, HSun⁺ and the CuSun complex as ligands.

Ligand	Binding Energy/kcal mol ^{−1}	K _i /μM
Sun	−4.71	355
HSun ⁺	−4.94	238
CuSun	−3.67	2030

The most favorable binding modes for Sun and HSun⁺ found by the docking simulations were in good agreement with the crystallized structure of sunitinib with the tyrosine kinase domain of VEGFR2, obtained by McTigue et al. [46]. The results in Table 4 show that HSun⁺ possess the most negative binding energy of the three compounds studied. Although Sun and HSun⁺ show very similar interactions between almost the same residues in the protein, slight conformational differences cause a more positive energy for the non-protonated state. Furthermore, while Sun forms only two hydrogen bonds in its lowest energy conformation, with Glu917 and Cys919 residues, HSun⁺ can form two additional hydrogen bonds, with Leu640 and Pro839 residues (Figure 4a), which explains, at least partially, its greater affinity for the receptor than Sun.

On the other hand, it can be seen from the data in Table 4 that the binding energy of CuSun is significantly more positive than that associated with the free ligands. Therefore, the results of the docking simulations seem to suggest that the complexation of sunitinib has a negative effect on the interactions between this drug and VEGFR2. Due to the mechanism of action of sunitinib, which competes with adenosine triphosphate (ATP) for the binding site analyzed here [47], the inhibitory activity of CuSun is expected to be lower than that associated with the free species. Although these results suggest that the complex obtained is not suitable for enhancing the antineoplastic effects of sunitinib with respect to its action on VEGFR2, a better understanding of this system could be gained by using molecular dynamics on CuSun and VEGFR2 since the latter considers not only the flexibility of the ligand, but also the ability of the receptor to move and react to it, and the results obtained in this way could potentially differ from those obtained by molecular docking. However, we have decided not to continue our studies in this direction, due to the poor affinity of the complex for the receptor compared to the free ligand, observed by the studies presented here.

A second binding site of VEGFR2 was tested using CuSun as a ligand. In this case, we have studied an allosteric site where certain inhibitors (such as sorafenib) bind, stabilizing an inactive form of the protein [48]. However, the binding energies calculated for the lowest energy conformations were even higher than those found for the ATP binding pocket, indicating poor affinity between the complex and this allosteric site, may be due to the proximity of a majority of hydrophobic residues like Leu840, Phe918, Leu1035, Leu1034, Val865, Val848, Val914, Phe1047, Ala866 and Cys919.

2.6. Cytotoxicity Study

Cytotoxicity studies were determined by the MTT assay for CuSun, Sun and Cu(NO₃)₂ (Biopack, Zárate, Argentina) as copper salt with HepG2 (hepatocarcinoma cells). Clinical agent sorafenib was used as clinical reference. Figure 5 shows that CuSun and Sun reduced the cell viability in the micromolar range of concentration (2.5–25 μM) on HepG2 cells whilst Cu⁺² did not exert anticancer effects. It is important to highlight that the anticancer activity of CuSun and Sun is quite similar. This result is in agreement to the speciation studies in which the complex dissociates in [CuCl₃(DMSO)][−] and HSun⁺. Besides, sorafenib impaired cell viability from very low concentration (2.5 μM) according to reported in literature [49].

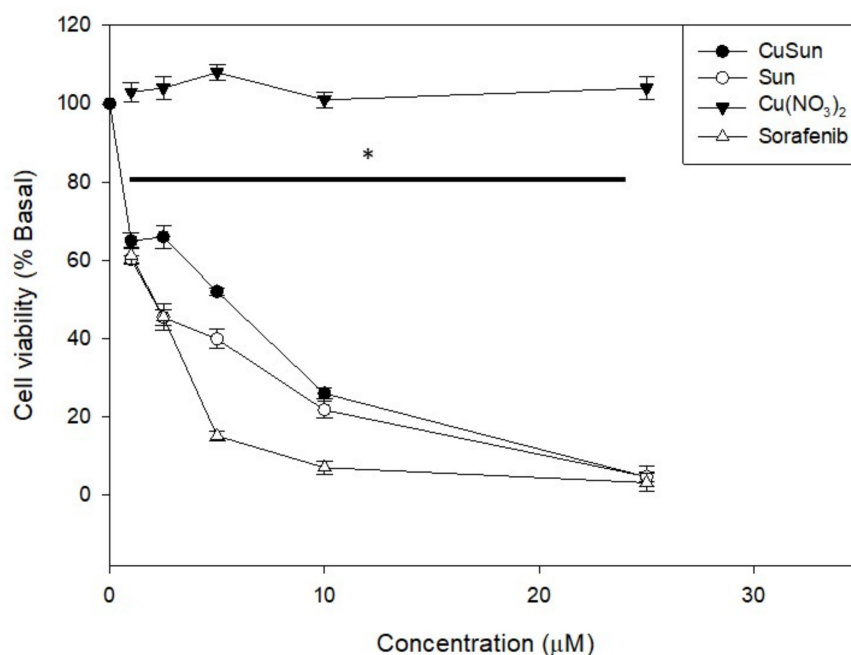


Figure 5. Cell viability of CuSun, Sun, Cu(NO₃)₂ and Sorafenib on HepG2 cancer cells. HepG2 cells were incubated in Dulbecco's modified Eagle's medium (DMEM) alone (control) or with different concentrations (1 to 25 µM) of Cu-SUT, SUT, Cu⁺² and Sorafenib. The results are expressed as the percentage of the basal level and represent the mean ± the standard error of the mean (SEM) (*n* = 18). * *p* < 0.01 differences between control and treatment.

3. Materials and Methods

3.1. Instruments, Reagents and Materials

All chemicals CuCl₂·2H₂O (Riedel de Hën, Seelze, Germany), acetone (Cicarelli, San Lorenzo, Argentina) and DMSO (Anedra, Buenos Aires, Argentina) were of analytical grade and used without further purification. Sunitinib: C₂₂H₂₇FN₄O₂ (Sun, Mw: 398.5 g/mol), was obtained from Shanghai Send Pharmaceutical Technology Co. Ltd. (Shanghai, China) and used without further purification. The polymorphic form A was identified in the yellow solid, since its DRX (Figure S8) was similar to reported in [50]. Diffuse reflectance spectrum: 295 nm and 428 nm (Figure S1). ¹HNMR (DMSO-d₆): 13.68 (s, 1H), 10.88 (s, 1H), 7.74–7.77 (m, 1H), 7.71 (s, 1H), 7.43–7.45 (m, 1H), 6.90–6.95 (m, 1H), 6.82–6.86 (m, 1H), 3.29 (m, 2H), 2.53–2.57 (m, 6H), 2.44 (s, 3H), 2.42 (s, 3H), 0.97–1.00 (t, 6H) (Figure S3).

FTIR spectra of powdered samples (as pressed KBr pellets) were measured with a Perkin Elmer (Waltham, Massachusetts, US) Spectrum BX FTIR-spectrophotometer from 4000 to 400 cm⁻¹, 32 scans, resolution ± 4 cm⁻¹. The dispersive Raman spectra were collected on a Horiba-Jobin-Yvon (Bensheim, Germany) T64000 Raman spectrometer, with a confocal microscope (100× objective) and CCD detection from 1770 to 100 cm⁻¹. A Kr laser with 647.1 nm of excitation wavelength and 50 mW power was used, resolution ± 1.5 cm⁻¹. Calibration was performed using the 459 cm⁻¹ band of CCl₄. For UV-vis determinations, a Shimadzu (Kyoto, Japan) UV-300 instrument, from 200 to 900 nm, spectral resolution 1 nm was used for both, diffuse reflectance (using MgO as an internal standard) and electronic absorption spectra (using 1 cm quartz cells). For conductimetric analysis, a digital Hanna edge EC conductivity meter was used, previously calibrated with KCl standard in 1413 µS cm⁻¹. Powder XRD was performed with a Rigaku (Tokyo, Japan) Microservo SR6402 diffractometer (wavelength 1.5405 Å), using the software Mercury 4.1.3. A Bruker (Billerica, Massachusetts, US) ESP300 spectrometer operating at the X-band was used to record the EPR spectrum of the complex at room temperature in the solid state and in solution. NMR spectra were acquired in a Bruker (Billerica, Massachusetts, US) with ¹H resonance of 400 MHz in DMSO-d₆. NMR chemical shifts are reported in ppm

with solvent residual signal as internal reference. Results were analyzed with the program MestReNova 14.2.0 (Mestrelab, Santiago de Compostela, Spain).

3.2. X ray Diffraction Data

The measurements were performed on a Rigaku-Oxford Gemini (Tokyo, Japan), Eos CCD diffractometer with graphite-monochromated MoK α ($\lambda = 0.71073 \text{ \AA}$) radiation. X-ray diffraction intensities were collected (ω scans with ϑ and κ -offsets), integrated and scaled with CrysAlisPro [51] suite of programs. The unit cell parameters were obtained by least-squares refinement (based on the angular setting for all collected reflections with intensities larger than seven times the standard deviation of measurement errors) using CrysAlisPro, Oxford Diffraction /Agilent Technologies UK Ltd., Yarnton, England. Data were corrected empirically for absorption employing the multi-scan method implemented in CrysAlisPro.

The structure was solved by intrinsic phasing with SHELXT [52] and the molecular model refined by full-matrix least-squares procedure with SHELXL [53]. All hydrogen atoms but the ones of methyl groups were located in a difference Fourier map and refined at their found positions with isotropic displacement parameters. The N(i)-H ($i = 2-4$) bond distances were restrained to a target value of $0.86(1) \text{ \AA}$. The methyl H-atoms were positioned at their expected geometrical locations and refined with the riding model. These H-atoms were treated as rigid groups allowed to rotate around the corresponding C-CH $_3$ bonds such as maximize the residual electron density at their respective calculated H-positions. Crystal data and structure refinement results are summarized in Table 1 and additional information are found in Tables S2–S5.

3.3. Computational Simulations

3.3.1. Hirshfeld Surface Analysis

The Hirshfeld surface of the CuSun complex was mapped with its different associated functions. In addition, the corresponding fingerprint plots were performed by using the CrystalExplorer 17.5 software [54], with the refined structure obtained by X-ray crystallography as the input.

3.3.2. Geometry Optimization of the CuSun Complex and FTIR Spectra Simulation

The electronic structure calculations were performed using Gaussian 16 (Rev. A03) package [55], by means of the Density Functional Theory (DFT). The starting geometry of the complex was obtained by X-ray crystallography. The results of several combinations of exchange-correlation energy functional and basis sets were assessed. We have considered the CAM-B3LYP functional, introduced by Yanai et al. [56], with LANL2DZ basis set on the Cu atom, and 6-311+G(d,p) on the non-metallic atoms, as the most suitable level of theory for the analysis of the CuSun complex. Sun was optimized at the same level. Then, the vibrational frequencies of their normal modes were calculated. The FTIR spectra of both, complex and free ligand in gas phase, were obtained from the results of the DFT calculations, by using Molden 5.8 software [57].

3.3.3. Molecular Docking with VEGFR2

The tyrosine kinase domain of VEGFR2 (PDB ID 3WZE, cocrystallized with sorafenib) was used as receptor. The protein was preconditioned, by removing the water molecules and other crystallized compounds (including sorafenib) and by checking for the presence of all amino acid residues in the vicinity of the binding sites. The polar hydrogen atoms were added using the Autodock 4.2.6 software package [58], and the protonation states of the histidine residues were checked individually. The atomic charges were assigned by using the Gasteiger model.

All ligands were previously optimized with Gaussian 16, at the CAM-B3LYP/6-311+G(d,p) level. Since Autodock 4.2.6 lacks a suitable model for the assignment of atomic charges on metal atoms, we have calculated them for all ligands (including those without Cu atoms), by means of the MK method using UFF atomic radii [59]. Due to the use of a

non-standard model for the partial charges, the binding energies obtained are suitable only for qualitative comparisons of the affinity of the ligands for the receptor.

To validate the proposed docking methodology, sorafenib was removed from its binding site in the crystallographic model, and this molecule was used as a flexible ligand in a first simulation. The grid box used had dimensions of $20.3 \times 20.3 \times 20.3 \text{ \AA}^3$, and a spacing of 0.203 \AA , centered on the allosteric site of the VEGFR2 kinase domain. The most favorable conformation observed was in excellent agreement with the crystallographic structure (Figure S9).

Subsequently, Sun was docked in its basic and protonated form, but in this case the grid box was centered on the ATP binding site of VEGFR2, also with a spacing of 0.203 \AA .

Certain inhibitors of VEGFR2 work by binding to the region that would otherwise be occupied by the adenine ring of an ATP molecule prior to the phosphorylation process, the ATP binding pocket (type I inhibitors, e.g., Sun). Others induce a conformational change in VEGFR2, stabilizing a non-active form of the protein, by binding to an allosteric site of it (type II inhibitors, e.g., sorafenib) [48,60]. CuSun was docked at both sites, using the same grid boxes mentioned above for sorafenib (allosteric site) and Sun (ATP binding pocket).

Due to the lack of copper parameters in Autodock 4.2.6 package we have used those proposed by Kathiresan et al. [61]. To assess the sensitivity of the results obtained with the parameters assigned to the metal atom, new docking simulations were carried out, but assigning the parameters associated with Zn and Mn (included in Autodock 4.2.6) to the Cu(II) atom of the CuSun. Because of this, no significant differences were observed in the most favorable poses, nor in the calculated binding energies (Table S6). This suggests that the results obtained are not very sensitive to the parameters used for the metal ion.

For every ligand, we have performed 1500 runs of a Lamarckian genetic algorithm, with a population of 300 individuals each, a maximum of 10^5 generations, one survivor per generation and a limit of 5×10^6 energy evaluations. The remaining parameters of the search algorithm were used by default. The standard Autodock 4.2.6 estimate for inhibition constants and binding energies was reported after cluster analysis with a RMSD of 2.5 \AA . The analysis and visualization of the results was performed using MGLTools and VMD 1.8.7 [62].

3.4. Cell Culture Conditions and Viability Studies

3.4.1. Cell Line and Growth Conditions

Human hepatocarcinoma cell line (HepG2, ATCC, HB-8065) was grown in Dulbecco's modified Eagle's medium (DMEM, Gibco; Thermo Fisher Scientific, Inc., Waltham, MA, USA) containing 10% fetal bovine serum (FBS, Internegocios S.A, Mercedes, Argentina), 100 IU/mL penicillin (Gibco; Thermo Fisher Scientific, Inc., Waltham, MA, USA) and 100 $\mu\text{g/mL}$ streptomycin (Gibco; Thermo Fisher Scientific, Inc., Waltham, MA, USA) at $37 \text{ }^\circ\text{C}$ in 5% CO_2 atmosphere.

3.4.2. Cell Viability Study

The MTT (3(4,5-dimethylthiazol-2-yl)-2,5-diphenyl-tetrazoliumbromide, Sigma Aldrich, Steinheim am Albuch, Germany) assay was performed according to Mosmann et al. [63] Briefly, cells were seeded in a 96-multiwell dish, allowed to attach for 24 h and treated with different concentrations of complex, ligand and free metal at $37 \text{ }^\circ\text{C}$ for 72 h. Afterward, medium was changed and cells were incubated with 0.5 mg/mL MTT under normal culture conditions for 3 h. Cell viability was marked by the conversion of the tetrazolium salt MTT to a colored formazan by mitochondrial dehydrogenases. Color development was measured spectrophotometrically in a microplate reader (model 7530, Cambridge technology, Inc., Cambridge, MA, USA) at 570 nm after cell lysis in DMSO ($100 \mu\text{L/well}$). Cell viability was plotted as the percentage of the control value.

4. Conclusions

In this work, we have synthesized and crystallized a tetrahedral coordination complex with copper(II) and protonated sunitinib ($\text{Cu}(\text{HSun})\text{Cl}_3$). By analyzing Hirshfeld surface, we have found π - π interactions and classic and non-classic H-bonds in the crystal structure. DFT calculations allowed us to predict the normal vibrational modes of the coordination complex and to propose a vibrational assignment for the experimental FTIR and Raman spectra. In DMSO solution, the complex has dissociated in protonated sunitinib and chloro-complex of copper(II), according to $^1\text{H-NMR}$, EPR, UV-vis and conductimetric analysis. In HepG2 cell line, no difference in cytotoxicity, by MTT assay, were found between complex and ligand in the range between 1–25 μM . Molecular docking of the complex in both, ATP binding site and allosteric site of VEGFR2 have shown no improvement in comparison to the free ligand.

Supplementary Materials: The following are available online at <https://www.mdpi.com/article/10.3390/inorganics10010003/s1>, Figure S1: Additional figures are UV-visible reflectance diffuse spectra, Figure S2: $^1\text{H-NMR}$ spectrum of CuSun, Figure S3: $^1\text{H-NMR}$ spectrum of Sun, Figure S4: band-X EPR spectra, Figure S5: fingerprint plots for CuSun, Figure S6: experimental and calculated FTIR spectra, Figure S7: experimental and calculated Raman spectra, Figure S8: XRD pattern, Figure S9: comparison between the docked and crystallographic structure for the VEGFR2-sorafenib complex. Table S1: Additional tables are H-bond distances and angles, Table S2: full bond distances and angles, Table S3: fractional coordinates and equivalent isotropic displacement parameters of the non-H atoms, Table S4: atomic anisotropic displacement parameters, Table S5: hydrogen atoms positions, Table S6: binding energy and inhibition constant for CuSun on VEGFR2 by molecular docking by using different parameters for the metal atom. Crystallographic structural data have been deposited at the Cambridge Crystallographic Data Centre (CCDC). Any request to the Cambridge Crystallographic Data Centre for this material should quote the full literature citation and the reference number CCDC 2088138.

Author Contributions: Conceptualization, I.E.L. and M.S.I.; Data curation, F.T., P.A.L. and M.S.I.; Formal analysis, F.T., I.E.L. and M.S.I.; Investigation, F.T., V.F., G.A.E., O.E.P., I.E.L. and M.S.I.; Methodology, F.T., P.A.L., V.F., G.A.E., O.E.P. and M.S.I.; Resources, P.A.L., S.G., I.E.L. and M.S.I.; Software, F.T. and P.A.L.; Supervision, I.E.L. and M.S.I.; Writing—original draft, F.T., P.A.L., O.E.P., I.E.L. and M.S.I.; Writing—review & editing, M.C., S.G., I.E.L. and M.S.I. All authors have read and agreed to the published version of the manuscript.

Funding: This research was partly funded by Universidad Nacional de La Plata (UNLP) (Grants X053 and 11/X857), Universidad Nacional de Mar del Plata (UNMDP) (Grants EXA 920/19 and EXA1022/21), Consejo Nacional de Investigaciones Científicas y Técnicas (CONICET) (PIP 0340 and PIP 0651), and Agencia Nacional de Promoción Científica y Tecnológica (ANPCyT) (PICT 2019-2322) from Argentina.

Acknowledgments: The authors thanks to Consejo Nacional de Investigaciones Científicas y Técnicas (CONICET) since G.A.E., O.E.P., M.S.I. and I.E.L. are members of the Researcher Career, P.A.L. is Postdoctoral Fellow and F.T. is Doctoral Fellow from the same institution.

Conflicts of Interest: The authors declare no conflict of interest.

References

1. Torre, L.A.; Bray, F.; Siegel, R.L.; Ferlay, J.; Lortet-Tieulent, J.; Jemal, A. Global cancer statistics, 2012. *CA Cancer J. Clin.* **2015**, *65*, 87–108. [[CrossRef](#)] [[PubMed](#)]
2. Kerbel, R.; Folkman, J. Clinical translation of angiogenesis inhibitors. *Nat. Rev. Cancer* **2002**, *2*, 727–739. [[CrossRef](#)] [[PubMed](#)]
3. Yang, J.C.; Haworth, L.; Sherry, R.M.; Hwu, P.; Schwartzentruber, D.J.; Topalian, S.L.; Steinberg, S.M.; Chen, H.X.; Rosenberg, S.A. A randomized trial of bevacizumab, an anti-vascular endothelial growth factor antibody, for metastatic renal cancer. *N. Engl. J. Med.* **2003**, *349*, 427–434. [[CrossRef](#)] [[PubMed](#)]
4. Ferrara, N.; Hillan, K.J.; Gerber, H.-P.; Novotny, W. Discovery and development of bevacizumab, an anti-VEGF antibody for treating cancer. *Nat. Rev. Drug Discov.* **2004**, *3*, 391–400. [[CrossRef](#)]
5. Willett, C.G.; Boucher, Y.; Di Tomaso, E.; Duda, D.G.; Munn, L.L.; Tong, R.T.; Chung, D.C.; Sahani, D.V.; Kalva, S.P.; Kozin, S.V.; et al. Direct evidence that the VEGF-specific antibody bevacizumab has antivascular effects in human rectal cancer. *Nat. Med.* **2004**, *10*, 145–147. [[CrossRef](#)]

6. Shaheen, R.M.; Tseng, W.W.; Davis, D.W.; Liu, W.; Reinmuth, N.; Vellagas, R.; Wiczorek, A.A.; Ogura, Y.; McConkey, D.J.; Drazan, K.E.; et al. Tyrosine kinase inhibition of multiple angiogenic growth factor receptors improves survival in mice bearing colon cancer liver metastases by inhibition of endothelial cell survival mechanisms. *Cancer Res.* **2001**, *61*, 1464–1468.
7. Bergers, G.; Song, S.; Meyer-Morse, N.; Bergsland, E.; Hanahan, D. Benefits of targeting both pericytes and endothelial cells in the tumor vasculature with kinase inhibitors. *J. Clin. Investig.* **2003**, *111*, 1287–1295. [[CrossRef](#)]
8. Ahmad, T.; Eisen, T. Kinase inhibition with BAY 43-9006 in renal cell carcinoma. *Clin. Cancer Res. Off. J. Am. Assoc. Cancer Res.* **2004**, *10*, 6388S–6392S. [[CrossRef](#)]
9. Abrams, T.J.; Lee, L.B.; Murray, L.J.; Pryer, N.K.; Cherrington, J.M. SU11248 inhibits KIT and platelet-derived growth factor receptor beta in preclinical models of human small cell lung cancer. *Mol. Cancer Ther.* **2003**, *2*, 471–478.
10. Mendel, D.B.; Laird, A.D.; Xin, X.; Louie, S.G.; Schreck, R.E.; Abrams, T.J.; Ngai, T.J.; Lee, L.B.; Murray, L.J.; Carver, J.; et al. In vivo Antitumor Activity of SU11248, a Novel Tyrosine Kinase Inhibitor Targeting Vascular Endothelial Growth Factor Receptors: Determination of a Pharmacokinetic/Pharmacodynamic Relationship. *Clin. Cancer Res.* **2003**, *9*, 327–337.
11. Carmeliet, P. VEGF as a key mediator of angiogenesis in cancer. *Oncology* **2005**, *69* (Suppl. 3), 4–10. [[CrossRef](#)]
12. Verheul, H.M.W.; Pinedo, H.M. The Role of Vascular Endothelial Growth Factor (VEGF) in Tumor Angiogenesis and Early Clinical Development of VEGFR Receptor Kinase Inhibitors. *Clin. Breast Cancer* **2000**, *1*, S80–S84. [[CrossRef](#)]
13. Lian, L.; Li, X.-L.; Xu, M.-D.; Li, X.-M.; Wu, M.-Y.; Zhang, Y.; Tao, M.; Li, W.; Shen, X.-M.; Zhou, C.; et al. VEGFR2 promotes tumorigenesis and metastasis in a pro-angiogenic-independent way in gastric cancer. *BMC Cancer* **2019**, *19*, 183. [[CrossRef](#)]
14. Guo, S.; Colbert, L.S.; Fuller, M.; Zhang, Y.; Gonzalez-Perez, R.R. Vascular endothelial growth factor receptor-2 in breast cancer. *Biochim. Biophys. Acta Rev. Cancer* **2010**, *1806*, 108–121. [[CrossRef](#)]
15. Committee for Medicinal Products for Human Use (CHMP). Sunitinib Accord Procedure No. EMEA/H/C/005419/0000. 2020. Available online: https://www.ema.europa.eu/en/documents/assessment-report/sunitinib-accord-epar-public-assessment-report_en.pdf (accessed on 21 December 2021).
16. Ferrari, S.M.; Centanni, M.; Virili, C.; Miccoli, M.; Ferrari, P.; Ruffilli, I.; Ragusa, F.; Antonelli, A.; Fallahi, P. Sunitinib in the Treatment of Thyroid Cancer. *Curr. Med. Chem.* **2019**, *26*, 963–972. [[CrossRef](#)]
17. Elgebaly, A.; Menshawy, A.; El Ashal, G.; Osama, O.; Ghanem, E.; Omar, A.; Negida, A. Sunitinib alone or in combination with chemotherapy for the treatment of advanced breast cancer: A systematic review and meta-analysis. *Breast Dis.* **2016**, *36*, 91–101. [[CrossRef](#)]
18. Pokuri, V.K.; Tomaszewski, G.M.; Ait-Oudhia, S.; Groman, A.; Khushalani, N.I.; Lugade, A.A.; Thanavala, Y.; Ashton, E.A.; Grande, C.; Fetterly, G.J.; et al. Efficacy, Safety, and Potential Biomarkers of Sunitinib and Transarterial Chemoembolization (TACE) Combination in Advanced Hepatocellular Carcinoma (HCC): Phase II Trial. *Am. J. Clin. Oncol.* **2018**, *41*, 332–338. [[CrossRef](#)]
19. Huang, J.; Zhang, X.; Tang, Q.; Zhang, F.; Li, Y.; Feng, Z.; Zhu, J. Prognostic significance and potential therapeutic target of VEGFR2 in hepatocellular carcinoma. *J. Clin. Pathol.* **2011**, *64*, 343–348. [[CrossRef](#)]
20. Lankheet, N.A.G.; Kloth, J.S.L.; Gadellaa-van Hooijdonk, C.G.M.; Cirkel, G.A.; Mathijssen, R.H.J.; Lolkema, M.P.J.K.; Schellens, J.H.M.; Voest, E.E.; Sleijfer, S.; de Jonge, M.J.A.; et al. Pharmacokinetically guided sunitinib dosing: A feasibility study in patients with advanced solid tumours. *Br. J. Cancer* **2014**, *110*, 2441–2449. [[CrossRef](#)]
21. Demlová, R.; Turjap, M.; Peš, O.; Kostolanská, K.; Juřica, J. Therapeutic Drug Monitoring of Sunitinib in Gastrointestinal Stromal Tumors and Metastatic Renal Cell Carcinoma in Adults—A Review. *Ther. Drug Monit.* **2020**, *42*, 20–32. [[CrossRef](#)]
22. Imbulgoda, A.; Heng, D.Y.C.; Kollmannsberger, C. Sunitinib in the Treatment of Advanced Solid Tumors. *Small Mol. Oncol.* **2014**, *201*, 165–184.
23. Anthony, E.J.; Bolitho, E.M.; Bridgewater, H.E.; Carter, O.W.L.; Donnelly, J.M.; Imberti, C.; Lant, E.C.; Lermyte, F.; Needham, R.J.; Palau, M.; et al. Metallodrugs are unique: Opportunities and challenges of discovery and development. *Chem. Sci.* **2020**, *11*, 12888–12917. [[CrossRef](#)]
24. Johnstone, T.C.; Suntharalingam, K.; Lippard, S.J. The Next Generation of Platinum Drugs: Targeted Pt(II) Agents, Nanoparticle Delivery, and Pt(IV) Prodrugs. *Chem. Rev.* **2016**, *116*, 3436–3486. [[CrossRef](#)]
25. Wang, D.; Lippard, S.J. Cellular processing of platinum anticancer drugs. *Nat. Rev. Drug Discov.* **2005**, *4*, 307–320. [[CrossRef](#)]
26. Leon, I.; Cadavid-Vargas, J.; Di Virgilio, A.; Etcheverry, S. Vanadium, Ruthenium and Copper Compounds: A New Class of Nonplatinum Metallodrugs with Anticancer Activity. *Curr. Med. Chem.* **2017**, *24*, 112–148. [[CrossRef](#)]
27. Gandin, V.; Ceresa, C.; Esposito, G.; Indraccolo, S.; Porchia, M.; Tisato, F.; Santini, C.; Pellei, M.; Marzano, C. Therapeutic potential of the phosphino Cu(I) complex (HydroCuP) in the treatment of solid tumors. *Sci. Rep.* **2017**, *7*, 13936. [[CrossRef](#)]
28. Denoyer, D.; Clatworthy, S.A.S.; Cater, M.A. 16. Copper complexes in cancer therapy. In *Metallo-Drugs: Development and Action of Anticancer Agents*; Sigel, A., Sigel, H., Freisinger, E., Sigel, R.K.O., Eds.; De Gruyter: Berlin, Germany, 2018; pp. 469–506.
29. Santini, C.; Pellei, M.; Gandin, V.; Porchia, M.; Tisato, F.; Marzano, C. Advances in Copper Complexes as Anticancer Agents. *Chem. Rev.* **2014**, *114*, 815–862. [[CrossRef](#)]
30. Balsa, L.M.; Ferraresi-Curotto, V.; Lavecchia, M.J.; Echeverría, G.A.; Piro, O.E.; García-Tojal, J.; Pis-Diez, R.; González-Baró, A.C.; León, I.E. Anticancer activity of a new copper(ii) complex with a hydrazone ligand. Structural and spectroscopic characterization, computational simulations and cell mechanistic studies on 2D and 3D breast cancer cell models. *Dalt. Trans.* **2021**, *50*, 9812–9826. [[CrossRef](#)]

31. Carcelli, M.; Tegoni, M.; Bartoli, J.; Marzano, C.; Pelosi, G.; Salvalaio, M.; Rogolino, D.; Gandin, V. In vitro and in vivo anticancer activity of tridentate thiosemicarbazone copper complexes: Unravelling an unexplored pharmacological target. *Eur. J. Med. Chem.* **2020**, *194*, 112266. [[CrossRef](#)]
32. Shobha Devi, C.; Thulasiram, B.; Aerva, R.R.; Nagababu, P. Recent Advances in Copper Intercalators as Anticancer Agents. *J. Fluoresc.* **2018**, *28*, 1195–1205. [[CrossRef](#)]
33. Shi, X.; Chen, Z.; Wang, Y.; Guo, Z.; Wang, X. Hypotoxic copper complexes with potent anti-metastatic and anti-angiogenic activities against cancer cells. *Dalt. Trans.* **2018**, *47*, 5049–5054. [[CrossRef](#)] [[PubMed](#)]
34. Balsa, L.M.; Baran, E.J.; León, I.E. Copper complexes as antitumor agents: In vitro and in vivo evidences. *Curr. Med. Chem.* **2021**. [[CrossRef](#)] [[PubMed](#)]
35. Ali, I.; Wani, W.A.; Saleem, K. Empirical Formulae to Molecular Structures of Metal Complexes by Molar Conductance. *Synth. React. Inorg. Met. Nano Metal Chem.* **2013**, *43*, 1162–1170. [[CrossRef](#)]
36. Elleb, M.; Meullemeestre, J.; Schwing-Weill, M.J.; Vierling, F. Spectrophotometric study of copper(II) chloride complexes in propylene carbonate and in dimethyl sulfoxide. *Inorg. Chem.* **1982**, *21*, 1477–1483. [[CrossRef](#)]
37. Meng, G.; Liu, C.; Qin, S.; Dong, M.; Wei, X.; Zheng, M.; Qin, L.; Wang, H.; He, X.; Zhang, Z. An improved synthesis of sunitinib malate via a solvent-free decarboxylation process. *Res. Chem. Intermed.* **2015**, *41*, 8941–8954. [[CrossRef](#)]
38. Kassem, M.G.; Motiur Rahman, A.F.M.F.M.; Korashy, H.M. Chapter 9—Sunitinib Malate. *Profiles Drug Subst. Excip. Relat. Methodol.* **2012**, *37*, 363–388.
39. Farrugia, L.J. WinGX and ORTEP for Windows: An update. *J. Appl. Crystallogr.* **2012**, *45*, 849–854. [[CrossRef](#)]
40. Spackman, M.A.; Jayatilaka, D. Hirshfeld surface analysis. *CrystEngComm* **2009**, *11*, 19–32. [[CrossRef](#)]
41. Clausen, H.F.; Chevallier, M.S.; Spackman, M.A.; Iversen, B.B. Three new co-crystals of hydroquinone: Crystal structures and Hirshfeld surface analysis of intermolecular interactions. *New J. Chem.* **2010**, *34*, 193–199. [[CrossRef](#)]
42. Kashinski, D.O.; Chase, G.M.; Nelson, R.G.; Di Nallo, O.E.; Scales, A.N.; VanderLey, D.L.; Byrd, E.F.C. Harmonic Vibrational Frequencies: Approximate Global Scaling Factors for TPSS, M06, and M11 Functional Families Using Several Common Basis Sets. *J. Phys. Chem. A* **2017**, *121*, 2265–2273. [[CrossRef](#)]
43. Mihçioğur, Ö.; Özpozan, T. Molecular structure, vibrational spectroscopic analysis (IR & Raman), HOMO-LUMO and NBO analysis of anti-cancer drug sunitinib using DFT method. *J. Mol. Struct.* **2017**, *1149*, 27–41. [[CrossRef](#)]
44. Alshetaili, A.S.; Anwer, M.K.; Alshahrani, S.M.; Alalaiwe, A.; Alsulays, B.B.; Ansari, M.J.; Imam, F.; Alshehri, S. Characteristics and anticancer properties of Sunitinib malate-loaded poly-lactic-co-glycolic acid nanoparticles against human colon cancer HT-29 cells lines. *Trop. J. Pharm. Res.* **2018**, *17*, 1263. [[CrossRef](#)]
45. Karimi, M.H.; Mahdavinia, G.R.; Massoumi, B. pH-controlled sunitinib anticancer release from magnetic chitosan nanoparticles crosslinked with κ -carrageenan. *Mater. Sci. Eng. C* **2018**, *91*, 705–714. [[CrossRef](#)]
46. McTigue, M.; Murray, B.W.; Chen, J.H.; Deng, Y.-L.; Solowiej, J.; Kania, R.S. Molecular conformations, interactions, and properties associated with drug efficiency and clinical performance among VEGFR TK inhibitors. *Proc. Natl. Acad. Sci. USA* **2012**, *109*, 18281–18289. [[CrossRef](#)]
47. Faivre, S.; Demetri, G.; Sargent, W.; Raymond, E. Molecular basis for sunitinib efficacy and future clinical development. *Nat. Rev. Drug Discov.* **2007**, *6*, 734–745. [[CrossRef](#)]
48. Modi, S.J.; Kulkarni, V.M. Vascular Endothelial Growth Factor Receptor (VEGFR-2)/KDR Inhibitors: Medicinal Chemistry Perspective. *Med. Drug Discov.* **2019**, *2*, 100009. [[CrossRef](#)]
49. Garten, A.; Grohmann, T.; Kluckova, K.; Lavery, G.G.; Kiess, W.; Penke, M. Sorafenib-Induced Apoptosis in Hepatocellular Carcinoma is Reversed by SIRT1. *Int. J. Mol. Sci.* **2019**, *20*, 4048. [[CrossRef](#)]
50. Konduri, S.K.M.; Satya, A.K.; Chowdary, N.V. Polymorphic Forms of Sunitinib Base. U.S. Patent 8,466,190, 18 June 2013.
51. Rigaku Oxford Diffraction. *CrysAlisPro Software System*; Version 1.171.38.41; Rigaku Corporation: Tokyo, Japan, 2015.
52. Sheldrick, G.M. SHELXT Integrated space-group and crystal-structure determination. *Acta Crystallogr. Sect. A* **2015**, *71*, 3–8. [[CrossRef](#)]
53. Sheldrick, G.M. A short history of SHELX. *Acta Crystallogr. Sect. A* **2008**, *64*, 112–122. [[CrossRef](#)]
54. Tan, S.L.; Jotani, M.M.; Tiekink, E.R.T. Utilizing Hirshfeld surface calculations, non-covalent interaction (NCI) plots and the calculation of interaction energies in the analysis of molecular packing. *Acta Crystallogr. Sect. E Crystallogr. Commun.* **2019**, *75*, 308–318. [[CrossRef](#)]
55. Frisch, M.J.; Trucks, G.W.; Schlegel, H.B.; Scuseria, G.E.; Robb, M.A.; Cheeseman, J.R.; Scalmani, G.; Barone, V.; Petersson, G.A.; Nakatsuji, H.; et al. *Gaussian 16*; Revision C.01; Gaussian, Inc.: Wallingford, UK, 2016.
56. Yanai, T.; Tew, D.P.; Handy, N.C. A new hybrid exchange–correlation functional using the Coulomb-attenuating method (CAM-B3LYP). *Chem. Phys. Lett.* **2004**, *393*, 51–57. [[CrossRef](#)]
57. Schaftenaar, G.; Noordik, J.H. Molden: A pre- and post-processing program for molecular and electronic structures*. *J. Comput. Aided. Mol. Des.* **2000**, *14*, 123–134. [[CrossRef](#)] [[PubMed](#)]
58. Morris, G.M.; Huey, R.; Lindstrom, W.; Sanner, M.F.; Belew, R.K.; Goodsell, D.S.; Olson, A.J. AutoDock4 and AutoDockTools4: Automated docking with selective receptor flexibility. *J. Comput. Chem.* **2009**, *30*, 2785–2791. [[CrossRef](#)] [[PubMed](#)]
59. Besler, B.H.; Merz, K.M.; Kollman, P.A. Atomic charges derived from semiempirical methods. *J. Comput. Chem.* **1990**, *11*, 431–439. [[CrossRef](#)]

60. Wang, Y.; Peng, C.; Wang, G.; Xu, Z.; Luo, Y.; Wang, J.; Zhu, W. Exploring binding mechanisms of VEGFR2 with three drugs lenvatinib, sorafenib, and sunitinib by molecular dynamics simulation and free energy calculation. *Chem. Biol. Drug Des.* **2019**, *93*, 934–948. [[CrossRef](#)]
61. Kathiresan, S.; Muges, S.; Murugan, M.; Ahamed, F.; Annaraj, J. Mixed-ligand copper (II)-phenolate complexes: Structure and studies on DNA/protein binding profiles, DNA cleavage, molecular docking and cytotoxicity. *RSC Adv.* **2016**, *6*, 1810–1825. [[CrossRef](#)]
62. Humphrey, W.; Dalke, A.; Schulten, K. VMD: Visual molecular dynamics. *J. Mol. Graph.* **1996**, *14*, 33–38. [[CrossRef](#)]
63. Mosmann, T. Rapid colorimetric assay for cellular growth and survival: Application to proliferation and cytotoxicity assays. *J. Immunol. Methods* **1983**, *65*, 55–63. [[CrossRef](#)]